

Light-induced oxygen-ordering dynamics in $(Y,Pr)Ba_2Cu_3O_{6.7}$: A Raman spectroscopy and Monte Carlo study

S. Bahrs, A. R. Goñi,* and C. Thomsen

Institut für Festkörperphysik, Technische Universität Berlin, Hardenbergstraße 36, 10623 Berlin, Germany

B. Maierov

Superconductivity Technology Center, MS K763, Los Alamos National Laboratory, Los Alamos, New Mexico 87545, USA

G. Nieva and A. Fainstein

Centro Atómico Bariloche, Comisión Nacional de Energía Atómica, 8400 San Carlos de Bariloche, Río Negro, Argentina

(Received 14 November 2003; revised manuscript received 11 May 2004; published 26 July 2004)

We investigated the time and temperature dependence of photobleaching effects in $RBa_2Cu_3O_{7-\delta}$ single crystals ($R=Y,Pr$) by Raman spectroscopy and Monte Carlo simulations based on the asymmetric next-nearest-neighbor Ising model. In a temperature range between 40 and 300 K the bleaching slows down on cooling, displaying a pronounced change in dynamics around 160 K for $R=Y$. To model this behavior we extended the Ising model by introducing a single energy barrier which impedes oxygen movement in the plane unless the oxygen atoms are excited by light. We obtain a time- and temperature-dependent development of superstructures under illumination with the fastest change at intermediate model temperatures. The chain-fragment development in the simulation thus matches the experimental low-temperature dynamics of Raman photobleaching, providing further support for oxygen reordering in the chain plane being at the origin of Raman photobleaching and related effects.

DOI: 10.1103/PhysRevB.70.014512

PACS number(s): 74.72.Bk, 78.30-j, 64.60.Cn, 73.50.Pz

I. INTRODUCTION

In oxygen-deficient $RBa_2Cu_3O_{7-\delta}$ a number of unusual effects observed with various methods are related to structural changes in the chain plane of the material. Samples quenched from high to about room temperature show spontaneous reordering of oxygen atoms in the chain sites on a time scale between hours and days.¹⁻³ The structural development has been monitored with x-ray and neutron scattering, both verifying a shortening of the crystallographic axes and the formation of superstructure patterns with full and empty chains for values of oxygen deficiency around $\delta \approx 0.5$.²⁻⁵ While the $R=Y$ compound has been the most thoroughly investigated, superstructure ordering has also been found for other $RBa_2Cu_3O_{7-\delta}$ materials.^{6,7} Along with this reorganization the critical temperature of the samples was observed to increase, pointing to the close connection between chain length and carrier concentration in the superconducting planes.² Calculations of the Cu1 valence in different oxygen surroundings explain the charge transfer involved.⁸ This correlation between structure and electrical properties has also been shown by application of pressure, after which the critical temperature also remains enhanced as long as the sample is kept cool, but relaxes when it is warmed up to room temperature.⁹ Other metastable effects are induced by illumination, such as persistent photoconductivity, where after exposure to visible light conductivity and, in superconducting samples, critical temperature show a metastable increase.¹⁰⁻¹⁴ Among the optical methods, Raman spectroscopy is particularly suitable for the investigation of oxygen reordering effects, as the spectra show a group of peaks related to vibrations of the chain oxygens, which lose intensity under illumination.¹⁵⁻²¹ Again, this change is stable at low

temperatures even after the illumination has been stopped, but reversible when the material is heated to room temperature.

While the relation between these experiments is not yet fully understood, some properties are remarkably similar. All effects occur only in samples with oxygen deficiency, they are frozen in (or metastable) at low temperatures but active (or reversible) at or above room temperature, the crossover being around 250 to 280 K. This range matches the glass transition of the thermal expansion coefficient found in underdoped material ($\delta \approx 0.1$), which was also assigned to a chain-forming contribution.²² Another common property is the functional form of the dynamics displayed in transport, annealing, and Raman experiments. All show a stretched exponential behavior, which is typical of disordered systems with a broad, statistical range of relaxation times and is often found in the context of glassy materials.

The reordering of oxygen atoms in the chain plane can account for at least part of these experimental observations. It has been shown that ordered superstructure patterns of full and empty chains in the chain plane are energetically favorable and provide a higher doping level of the superconducting planes than statistically distributed vacancies.⁸ The structural phase diagram of $YBa_2Cu_3O_{7-\delta}$ has been simulated with the Monte Carlo based asymmetric next nearest neighbor Ising (ASYNNNI) model as developed, e.g., by Andersen *et al.*^{5,23-27} For spontaneous oxygen reordering above room temperature, x-ray and neutron diffraction provide direct evidence for the link of transport properties to axis shortening and superstructure development.²⁻⁵ Both pressure and illumination reduce the c -axis length and increase the critical temperature due to the charge transfer they induce.^{9,28} This suggests that the microscopic process is similar to that for

spontaneous reordering. With decreasing temperature, this spontaneous reordering freezes.

Although the precise origin of the Raman signal with its uncommon bleaching behavior is not fully understood, the relationship to the Cu-O-chain plane is evident. First, the Raman peaks appear in oxygen-deficient material only, reaching their peak intensity around $\delta=0.3$.¹⁸ Their selection rules are such that they appear only with incident and detected light polarization parallel to the chain direction; a Raman tensor with this symmetry does not exist in the ideal crystal.²⁹ Second, an isotope site selective experiment with ¹⁸O displayed a frequency shift appropriate for substitutions in the most easily affected chain plane.³⁰ The bleaching effect as well is triggered solely by light polarized along the chain direction.^{15,31} Several mechanisms of Raman activation have been discussed, which are all related to chain formation and defect sites in the chains due to oxygen vacancies.^{15,17,18,20,31}

This motivated us to study in detail the bleaching dynamics and its temperature dependence, and to model the chain-fragment development for comparison with our Raman results. Our working hypothesis is that light excitation revives the site changes of oxygen atoms, enabling reordering *below* the threshold temperature on a time scale observable in the laboratory. Raman spectroscopy is sensitive to this structural change rather than to changes in the carrier concentration or mobility.

In this paper we present a detailed investigation of the temperature dependence of Raman bleaching in the range between 40 and 300 K of the reversible oxygen ordering effects in $\text{YBa}_2\text{Cu}_3\text{O}_{6.7}$ and $\text{PrBa}_2\text{Cu}_3\text{O}_{6.7}$ single crystals. The time constants vary drastically with temperature, showing much faster decay for $R=\text{Pr}$ and a remarkable change of behavior for $R=\text{Y}$ around 160 K. Using an adapted ASYNNI Monte Carlo simulation we explain the form of decay and its variation with temperature in terms of oxygen reordering via neighboring site hopping in the chain plane.

A brief description of the sample preparation and the details of the Raman setup in Sec. II is followed by the time- and temperature-dependent Raman results in Sec. III. In Sec. IV we introduce the simulation setup and compare the simulation results to the Raman decay.

II. EXPERIMENTAL DETAILS

For the Raman experiments samples of crystalline $\text{YBa}_2\text{Cu}_3\text{O}_{6.7}$ were prepared using the flux-growth technique with yttria stabilized ZrO_2 trays. The method and proportions were the same as in Ref. 32. The chosen crystal was subsequently detwinned under uniaxial stress as described elsewhere.²⁰ The same procedure was used to grow the $\text{PrBa}_2\text{Cu}_3\text{O}_{6.7}$ sample, with special care to choose single crystals with no Y contamination from the trays. The oxygen content reduction for the Y and Pr samples were performed at 507 °C in an oxygen atmosphere of 14.5 mbar followed by a controlled cooling down process.³³

The samples were kept at room temperature in the dark for several weeks and quenched from 293 K to low temperatures with a cooling rate of 20 K/min using an Oxford cry-

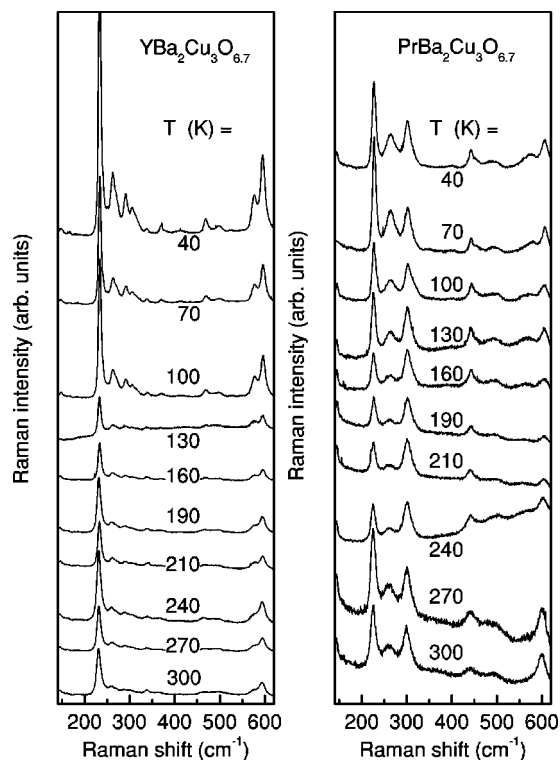


FIG. 1. Raman spectra of an $\text{YBa}_2\text{Cu}_3\text{O}_{6.7}$ untwinned single crystal (left) and a twinned $\text{PrBa}_2\text{Cu}_3\text{O}_{6.7}$ single crystal (right) for various temperatures, taken in $z(yy)z$ geometry ($y=b$ for $R=Y$) with the 568 nm line, $P_\lambda=6$ mW laser power, and an integration time of 45 min. The spectra have been normalized to the intensity of the B_{1g} -like mode at 339 and 301 cm^{-1} for $R=Y$ and Pr, respectively, and offset for clarity.

ostat. All bleaching Raman measurements were recorded in backscattering geometry on a previously unilluminated spot of the sample using a triple grating spectrometer equipped with a nitrogen cooled charge-coupled device detector. For excitation the 568 nm line (power $P_\lambda=6$ mW outside the cryostat) of an Ar⁺-Kr⁺ laser was focused on a spot of about 100 μm in diameter. The laser light served as excitation as well as for bleaching the samples. The bleaching was observed by taking sequential spectra with an accumulation time of 90 s for a total illumination period of 45 min.

III. EXPERIMENTAL RESULTS

A. Raman spectra

Raman spectra of an untwinned single crystal of $\text{YBa}_2\text{Cu}_3\text{O}_{6.7}$ and a twinned single crystal of $\text{PrBa}_2\text{Cu}_3\text{O}_{6.7}$ at various temperatures are shown in Fig. 1. The spectra were taken with an excitation wavelength of $\lambda=568$ nm, which is at the center of a resonance [full width at half maximum 160 meV (Ref. 15)] found in the material containing Y. For the structurally similar compound $R=\text{Pr}$ the profile, to our knowledge, has not been determined, but we assume it to be similar. In the $\text{YBa}_2\text{Cu}_3\text{O}_{6.7}$ spectra, intense defect-induced modes with two groups of peaks at 232, 263, 291 and 306, and 576 and 596 cm^{-1} are dominant compared to the Raman-

allowed modes at 339, 469, and 498 cm^{-1} .²⁹ While being very distinct at low temperatures, they change around 160 K into broader, washed out, and smaller forms. At temperatures above 250 K the satellite peaks of the largest defect feature at 232 cm^{-1} become indistinguishable. Thermally induced oxygen hopping becomes active in that temperature range, indicating a connection. For $\text{YBa}_2\text{Cu}_3\text{O}_{6.7}$ the defect-related peaks are more pronounced at low temperatures ($T < 130$ K) because of the larger time constants for bleaching. All defect-induced peaks behave similarly in their temporal development; hence we take them to be connected to the same physical origin. In the $\text{PrBa}_2\text{Cu}_3\text{O}_{6.7}$ spectra, the defect-induced peaks are found at 228, 264, 573, and 607 cm^{-1} , and the Raman-allowed modes at 301, 443, and 490 cm^{-1} . Allowed and defect-induced peaks have comparable intensity, possibly because of poorer resonant conditions for $R=\text{Pr}$. The shape and number of peaks change little with temperature; only the features at 264 and 576 cm^{-1} become more pronounced at low temperatures. Different intensities in the time integrated spectra of Fig. 1 are again caused by different decay rates.

Although the relation to the chains is known, the activation mechanism for the defect peaks has not yet been clarified.^{17,18,20,21,31} One possibility which accounts for the large number of peaks as well as their joint bleaching is that the structures reflect the partial density of states when the chains and symmetry are broken.

Figure 2 shows sequential spectra of 90 s integration time of the two samples at $T=40$ K, starting at the top, to 45 min total illumination time at the bottom. While all defect-induced peaks decrease in intensity, the Raman-allowed modes remain constant; see, e.g., the B_{1g} -like mode at 301 cm^{-1} in the $\text{PrBa}_2\text{Cu}_3\text{O}_{6.7}$ sample. The peaks recover to their original intensity when annealed at room temperature in the dark, but a time-dependent tracing of the process using Raman spectroscopy is obviously impossible.¹⁵

B. Time-dependent Raman bleaching

Figure 3 shows the large temperature dependence of the intensity of the largest defect-induced Raman feature (at 232 cm^{-1} in $\text{YBa}_2\text{Cu}_3\text{O}_{6.7}$ and at 228 cm^{-1} in $\text{PrBa}_2\text{Cu}_3\text{O}_{6.7}$) versus illumination time. For a more detailed description, parameters are extracted from the curves in Fig. 3 using a stretched exponential function, which is typical for heavily disordered systems, to describe the Raman intensity:³⁴

$$I(t) = I_0 \exp \left[- \left(\frac{t}{\tau} \right)^\beta \right] + \text{const.} \quad (1)$$

The fit parameters are given in Fig. 4. In a different Raman investigation on $\text{YBa}_2\text{Cu}_3\text{O}_{7-\delta}$ by Panfilov *et al.*, a simple exponential function was used; however, it does not describe our data well, as we clearly find $\beta < 1$.¹⁸ A small value for β corresponds to curves with high initial steepness and flat asymptotic behavior compared to a simple exponential function. The decay times τ are displayed in Fig. 4(a), showing that the decay becomes much faster with increasing temperature. In the case of $R=\text{Y}$, the decay times exceed the duration of the experiment (45 min) for the lowest temperatures in-

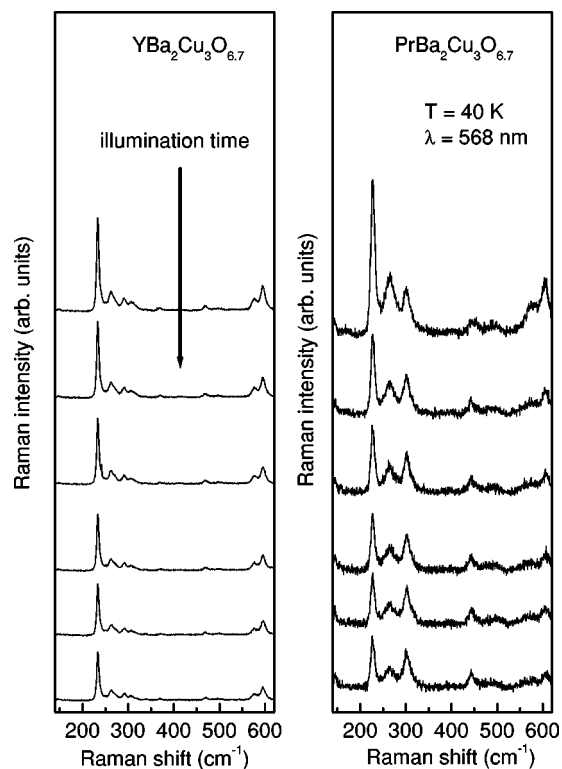


FIG. 2. Sequential Raman spectra of $\text{YBa}_2\text{Cu}_3\text{O}_{6.7}$ (left) and $\text{PrBa}_2\text{Cu}_3\text{O}_{6.7}$ (right) taken with $\lambda=568$ nm and $P=6$ mW, integration 90 s at a temperature of 40 K. The spectra have been offset for clarity, beginning at the top down to 45 min illumination time at the bottom. The defect peaks decrease while Raman-allowed modes remain unaltered.

vestigated. The Raman intensity in $R=\text{Pr}$ decreases faster by an order of magnitude in comparison to Y , in accordance with our previous findings in an investigation on a set of samples with different R at fixed temperature.²¹ While $\text{PrBa}_2\text{Cu}_3\text{O}_{6.7}$ as the only nonsuperconducting member of the $R\text{Ba}_2\text{Cu}_3\text{O}_{7-\delta}$ family might be expected to be exceptional, we found in previous investigations that its shorter decay time is in accordance with the other $R\text{Ba}_2\text{Cu}_3\text{O}_{7-\delta}$ compounds. $\text{PrBa}_2\text{Cu}_3\text{O}_{6.7}$ has a considerably larger unit cell and is more tetragonal than $\text{YBa}_2\text{Cu}_3\text{O}_{7-\delta}$. Both oxygen-atom mobility in the chain plane and the chain-building tendency are then different. The faster decay indicates lower barriers against oxygen hopping.

The exponent β is shown in Fig. 4(b). Interestingly, for $R=\text{Y}$ the shape of the bleaching curves changes toward a steeper beginning and flattened end at temperatures above about 160 K, which is reflected in a pronounced change of β between two fairly constant values [0.70 and 0.35 (± 0.05); full symbols in Fig. 4(b)]. We found the same property in previous experiments on ceramic $\text{YBa}_2\text{Cu}_3\text{O}_{7-\delta}$ samples.³¹ $\text{PrBa}_2\text{Cu}_3\text{O}_{6.7}$ [open symbols in Fig. 4(b)], in contrast, shows constant $\beta=0.35$ (± 0.05). It remains an open question whether $\text{PrBa}_2\text{Cu}_3\text{O}_{6.7}$ does not display a change in β at all, or the corresponding temperature threshold is below the reach of our investigation.

The change of decay in that temperature range points to a change in the type of dynamics, or maybe to an energy bar-

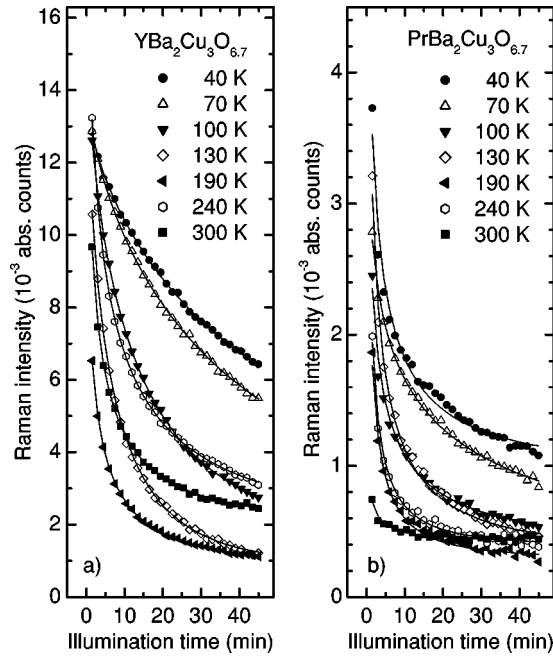


FIG. 3. Decrease of the Raman intensity of the peak at 232 cm^{-1} in the untwinned $\text{YBa}_2\text{Cu}_3\text{O}_{6.7}$ (a), and at 228 cm^{-1} in the twinned $\text{PrBa}_2\text{Cu}_3\text{O}_{6.7}$ sample (b) under illumination for various temperatures. Solid lines are fits to Eq. (1); for the fit parameters see Fig. 4.

rier comparable to the thermal energy. Freezing temperatures for thermally activated oxygen hopping deduced from transport measurements and x-ray monitoring of the structural parameters are considerably higher [above 280 K (Ref. 12)]. We therefore conclude that illumination-induced oxygen hopping in $\text{YBa}_2\text{Cu}_3\text{O}_{6.7}$ is governed by a different, smaller energy barrier than thermally induced reordering.

The curves in Fig. 3 show that a slow decay at low temperatures is combined with high starting points in the first illumination time interval. We mentioned the different initial amplitudes in connection with Fig. 1. This behavior is a consequence of the finite accumulation time of 90 s for the first spectrum of a series. The initial intensities extrapolated from the fits [Fig. 4(c)] are roughly constant, showing even a slight increase toward higher temperatures for $R=Y$.

The high-temperature decay ends at higher values of peak intensity than some of the intermediate decays: the most efficient bleaching occurs at 190 K in our experiments. This is best seen in Fig. 4(d), where we put the background values (the constant in the stretched exponential fit equation) from the fits as well as the last data point of each set. A discrepancy between these two values indicates that the decay is far from equilibrium. A comparison emphasizes what is obvious from the decay times already: Most of the dynamics are completed within the experimental time span of 45 min. Only for the two lowest temperatures ($T < 70\text{ K}$) in $R=Y$ is the decay slowed down so much that large uncertainties of the fit parameters result.

In the oxygen-reordering model these results can be read as follows. The intensity of defect-induced Raman peaks can, quite independently of the actual activation mechanism, be a measure for the density of symmetry breaches in oxygen-

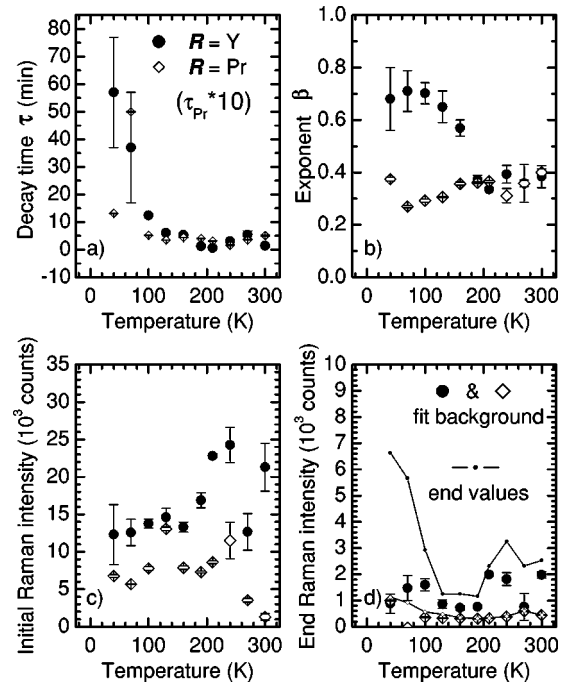


FIG. 4. Parameters from the fits in Fig. 3; full symbols correspond to $\text{YBa}_2\text{Cu}_3\text{O}_{6.7}$, open symbols to $\text{PrBa}_2\text{Cu}_3\text{O}_{6.7}$. (a) Decay time τ (note that the values for Pr have been multiplied by 10), (b) exponent β , (c) initial intensity, and (d) end intensity from fit and actual last value of the sequence (lines).

deficient $R\text{Ba}_2\text{Cu}_3\text{O}_{7-\delta}$. The symmetry is disturbed where a missing oxygen atom interrupts a Cu-O chain, which is translation invariant and not Raman active in the ideal structure. Illumination decreases the Raman intensity, so the number of open chain ends must be reduced by the development of longer full or completely empty chains at the expense of short fragments. This implies that light excitation enables oxygen diffusion in the plane in a temperature region where thermally activated movement is frozen. At low temperatures, it is reasonable that the equilibrium state is more ordered than the frozen-in high-temperature configuration. However, the Raman decay shows a temperature dependence with the most efficient bleaching occurring at intermediate temperatures, indicating a nonmonotonic, more complex dynamical dependence. In order to discuss this decay data in more detail in terms of the oxygen-reordering model we set up a simulation of chain fragments in a two-dimensional grid.

IV. SIMULATIONS

Monte Carlo simulations using neighboring-site hopping (Kawasaki dynamics) on a two-dimensional grid were done in order to describe the form and temperature dependence of Raman intensity decay in the oxygen-reordering model. A description of the anisotropic chain plane interactions in $\text{YBa}_2\text{Cu}_3\text{O}_{6.7}$ is provided by the two-dimensional (2D) asymmetric next nearest neighbor model as developed, for example, by Andersen *et al.* in Ref. 5. They were able to model the structural phase diagram including the ortho-III phase,

which is probably the relevant case for our oxygen concentration, with a set of four parameters. We base our calculations on this setup, although there has been much work on a more detailed description.^{23–27} The dynamical properties of the ASYNNI model and oxygen reordering have been studied in detail in Refs. 35–38, focusing on the range of thermally induced reordering above room temperature. Below room temperature, Federici *et al.* have shown that a stretched exponential decay of illumination-induced change in transport experiments can be obtained using a cellular automata model.¹³ Our aim is the modeling of the main dynamical process of the pattern building for a fixed oxygen deficiency matching our samples, explaining the properties of the low-temperature Raman decay within the picture of light-induced oxygen reordering.

Following the arguments from Sec. I and conclusions from Sec. III, we make the following assumptions for the model. The Raman intensity of the defect-induced peaks is taken as a measure of fragmentation in the Cu-O chain plane of $R\text{Ba}_2\text{Cu}_3\text{O}_{7-\delta}$. Light excitation enables reordering of oxygen vacancies within the chain plane at low temperatures, analogous to the thermally activated effect observed at higher (room) temperature. As in persistent photoconductivity relaxation, an energy barrier is associated with the thermally activated recovery process.^{12,14} Therefore, an energy barrier is introduced in the simulations, resulting in “frozen disorder” when the simulation is quenched from high temperatures. Illumination triggers further reordering at low temperatures by disabling that barrier. The fragment number is then monitored and compared for different temperatures during the simulation, showing the development from a frozen-in disordered state toward the equilibrium state.

A. Simulation setup and general properties

The next-nearest-neighbor interaction energies for four sites relative to an oxygen position are defined in Fig. 5. The left panel represents part of a Cu-O-chain plane in an Y123 crystal structure, with the solid-line circles marking the positions of Cu1 atoms at the four corners of a unit cell and the dashed circles representing possible oxygen atom sites. In all simulations presented we use the values for the interaction parameters V_i obtained by Andersen *et al.* in their simulation of the experimental phase diagram of $\text{YBa}_2\text{Cu}_3\text{O}_{7-\delta}$: $V_1/k_B = 5430$ K, $V_2 = -0.36V_1$, $V_3 = 0.12V_1$, and $V_4 = 0.04V_1$.⁵ All interaction energies except for the one favoring chain connections across Cu atoms are repulsive, being strongest for the smallest distance on sites in a and b direction in the same unit cell. The resulting summation of interaction energy terms gives:

$$E = -V_1 \sum_{(r,r')} \sigma(r)\sigma(r') - V_2 \sum_{(r,r')} \sigma(r)\sigma(r') - V_3 \sum_{(r,r')} \sigma(r)\sigma(r') - V_4 \sum_{(r,r')} \sigma(r)\sigma(r'), \quad (2)$$

with $\sigma(r)$ and $\sigma(r')$ being one for occupied sites and zero otherwise, and the sum running up to the number of nearest- and next-nearest-neighbor sites as defined in the left panel of

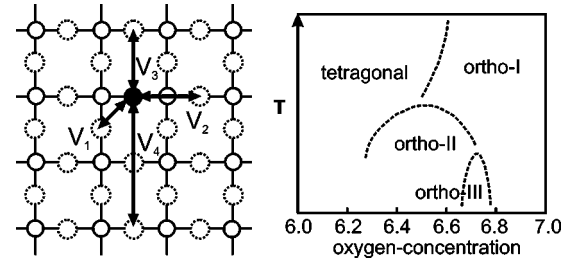


FIG. 5. Left panel: Part of the Cu-O chain plane of a high- T_c superconductor of the $R\text{Ba}_2\text{Cu}_3\text{O}_{7-\delta}$ type (solid lined circles are Cu, dotted circles represent possible oxygen sites) with the interaction parameters for possible neighboring positions of the oxygen atom indicated (filled circle). Right panel: Schematic phase diagram of $\text{YBa}_2\text{Cu}_3\text{O}_{7-\delta}$ structure, oxygen content versus temperature. The transition between ortho-II and ortho-I for $\delta=0.5$ occurs at about 385 K (Ref. 5).

Fig. 5. We used a 120×120 oxygen site matrix with periodic boundary conditions. All simulations started with a randomly chosen configuration, which was annealed to equilibrium at $180 \times 10^{-3} V_1/k_B$ simulation temperature. After annealing, it was quenched to the temperature of interest and left for 3×10^7 Monte Carlo steps for the entire ensemble.

The right panel of Fig. 5 displays a schematic diagram of the resulting structural phases at different oxygen concentrations $7 - \delta$. The original simulation as well as our setup yield those patterns, as seen from the real space and fast Fourier transform plots in Fig. 6. Randomly distributed fragments in the tetragonal phase [Fig. 6(a)] are opposed to orthorhombic patterns at higher oxygen occupation [ortho-II, ortho-III, and ortho-I in Figs. 6(b)–6(d), respectively] with the corresponding peaks in the reciprocal lattice space. For all phases twinning can occur. We see such a twinning in Fig. 6(c) with the domain boundary running vertically through the middle of the panel, while the phase shown in 6 (d) is untwinned. The Cu-O chain direction defines which axis is referred to as the b axis of a domain. The crystal’s a and b axes run diagonally in our simulation pictures of Fig. 6 for technical reasons. We give the temperature in units of the strongest interaction energy V_1 , since it sets the scale for the temperature dependence (as a reference, $100 \times 10^{-3} V_1/k_B = 543$ K for V_1 chosen as in Ref. 5).

In addition to the static model setup, the dynamics is chosen to model the movement of oxygen atoms in the planes (Kawasaki dynamics). In a Metropolis step an oxygen atom can change to a nearest-neighbor site (corresponding to a V_1 relative position in Fig. 5), or to a next-nearest-neighbor position corresponding to the V_3 direction. The two kinds of jumps are treated identically and the total number of oxygen atoms in a simulation is constant.

Figure 7(a) shows the number of fragments at the end of a simulation for various oxygen fillings of the lattice versus simulation temperature. All chains are counted, independent of direction or length. This includes “single” oxygen atoms, because they constitute a structure with a defined direction in the plane together with the neighboring copper atoms. The number of fragments is related to the number of atoms in the matrix as well as to the degree of chain formation. At temperatures comparable to the interaction energies, the latter

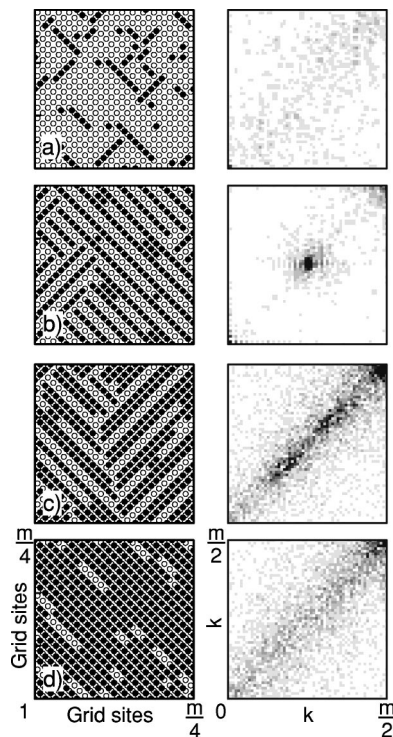


FIG. 6. Part of simulated Cu-O chain planes of size m^2 , $m = 120$, after 10^4 Monte Carlo steps/site for various concentrations of oxygen atoms (full symbols) in the copper grid (open symbols), from different parts of the structural phase diagram in Fig. 5. One quadrant of their Fourier transformations, corresponding to one twin direction, is shown to illustrate their regularity. Zero reciprocal lattice vector is at the lower left, the maximum at the upper right corner of the plots. The crystallographic axes a and b run along the diagonals. (a) $\delta=0.80$, $T=370 \times 10^{-3} V_1/k_B$, tetragonal phase; (b) $\delta=0.50$, $T=95 \times 10^{-3} V_1/k_B$, ortho-II-phase; (c) $\delta=0.33$, $T=55 \times 10^{-3} V_1/k_B$, ortho-III-phase; (d) $\delta=0.15$, $T=90 \times 10^{-3} V_1/k_B$, ortho-I-phase.

process is dominant. Consequently, the lowest fragment numbers are found for a filled lattice, where chain formation is almost perfect up to temperatures of the order of V_1/k_B . There the chains disintegrate and the number of fragments rises quickly. For oxygen-reduced lattices, the fragmentation is high because short chains exist statistically distributed. When temperatures get low enough, the smaller interactions $V_{2,3,4}$ set in and superstructure patterns develop, lengthening the fragments and decreasing their number further. For very low simulation temperatures, we encounter thermal freeze-out. As a result, equilibrium is not reached within the simulation time and the number of fragments remains high below $70 \times 10^{-3} V_1/k_B$. Pattern building and freeze-out in the simulations thus restrict the temperature range for comparison to experiment.

To account for the metastable photoexcitation state a tunable frozen state is needed in the model. It is introduced as an energy barrier E_B , which has to be overcome in a site change. Effectively, the barrier reduces the oxygen hopping rate by a value that depends only on temperature. Figure 7(b) shows how increasing E_B pushes the freeze-out point toward higher temperatures. We chose a value of $0.32V_1$, matching

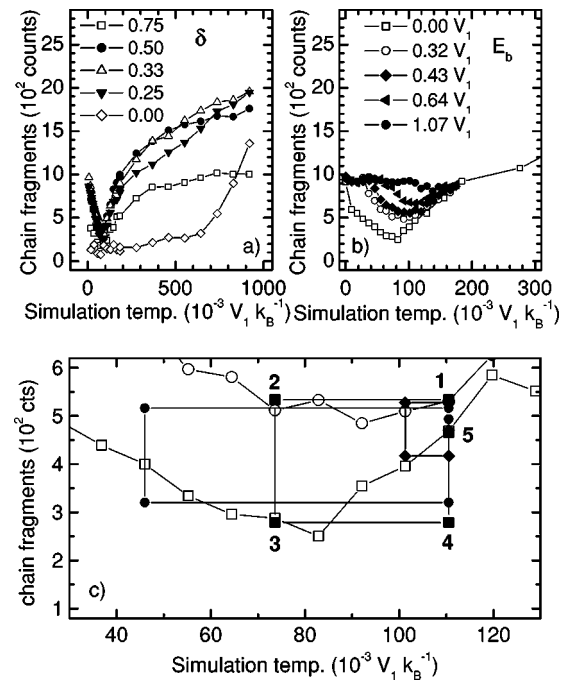


FIG. 7. Total number of fragments in the simulation after equilibration. (a) For different oxygen concentrations; $\delta=0$ refers to zero oxygen deficiency, $\delta=1$ to an empty lattice. (b) Simulation for energy barriers of 0 (open squares), 0.32 (open circles), 0.43 (filled rhombi), 0.68 (filled triangles), and $1.07V_1$ (filled circles). (c) Open symbols represent fragment numbers after simulation with zero barrier (open squares) and $E_B=0.32V_1$ (open circles) reproduced from (b) for comparison. Full symbols show simulation cycles of the modeling of bleaching for three different temperatures. The process of bleaching is modeled as a simulation run at a temperature of $0.11V_1/k_B$ (point 1) and then setting a lower simulation temperature (point 2). Then the energy barrier is diminished as a consequence of light excitation (to point 3). Finally, warming up again (point 4) enables relaxation (point 5).

the interaction parameters, to ensure that temperatures for which equilibrium is reached overlap with temperatures of superstructure-pattern development. The experiment suggests that the energy barrier under illumination should be significantly smaller. In a first approximation, we take it to be zero. Illumination is then simply modeled as a reduction of the barrier to zero for all oxygen atoms considered for a site change.

A simulation cycle emulating bleaching runs as shown in Fig. 7(c). For comparison, the two curves indicated by open symbols are simulation results for zero energy barrier and for $E_B=0.32V_1$ reproduced from Fig. 7(b). The three sets of full symbols represent sequential simulations modeling the Raman-bleaching process at three different temperatures. We begin with a random, annealed distribution at an upper temperature of $110 \times 10^{-3} V_1/k_B$ [point 1 in Fig. 7(c)]. The resulting oxygen matrix is a twinned region of ortho-III phase shown in Figs. 8(a) and 8(d), similar to the one in Fig. 6(c). Then the temperature is lowered to the range where little or no oxygen site change occurs due to the energy barrier imposed and the system is frozen [point 2 in Fig. 7(c)]. Subsequently, light is switched on, simply increasing the hopping

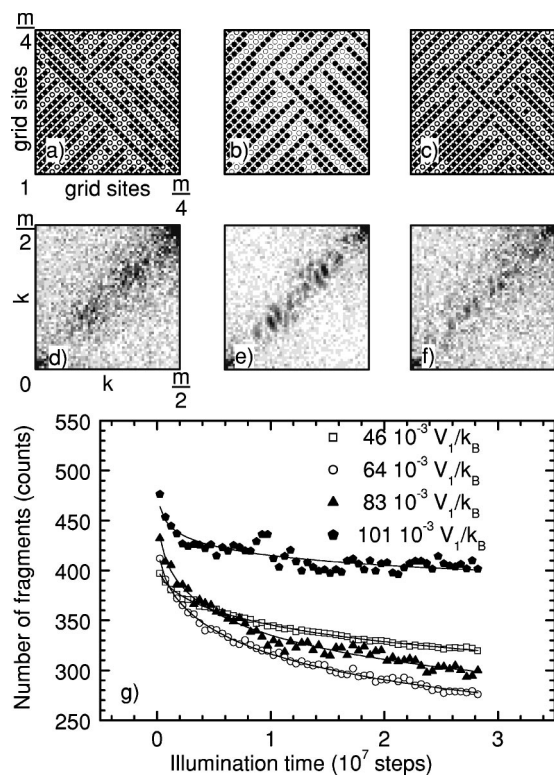


FIG. 8. (a), (b), and (c) show part of the matrices for $0.07V_1/k_B$, before and after illumination and after warming. (e), (f), and (g) display an increase of ortho-III pattern fractional peaks in the corresponding 2D Fourier transformations. (g) Number of chain fragments in a 120×120 simulation for simulation temperatures between $1/6$ and full initial annealing temperature.

rate at low temperatures by setting the barrier to zero [moving to point 3 in Fig. 7(c)]. The matrix developing under illumination is displayed in Figs. 8(b) and 8(e), showing a more pronounced O-III pattern. Finally, the oxygen matrix is set back to the initial temperature and value of the energy barrier [Fig. 7(c), point 4] from where it recovers to a state of increased disorder [point 5 in Fig. 7(c), matrices Figs. 8(c) and 8(f)], and the cycle is completed. Of these stages, the development from point 2 to point 3 corresponds to the bleaching of the Raman experiments. The other two cycles in Fig. 7(c) illustrate the effect of moving this stage to higher or lower temperatures.

Note that with the interaction values V_i of the literature there is no one-to-one match of the actual temperatures in the experiment. Moving the simulation cycle down to the appropriate temperatures is hindered by the critical slowing-down effect of the algorithm and would require much longer calculations. Similarly, we used only $0.32V_1$ instead of a barrier of about 1 eV. The static model we adopted was calibrated using the phase diagram, providing a set of correctly related parameters for the structural anisotropy which is the driving force of chain development in the first place. The energy barrier deduced from the transport experiments is an order of magnitude larger than the interaction energies and would freeze the simulation above the superstructure temperature range. Also, we do not impose a calibration of the time scale in the dynamical simulations, because this would require

some independent information about the excitation rate and hopping cross section. However, we obtain a reasonable order of magnitude by assuming an absorption rate in the experiment [laser power of 3 mW in a volume of 100 nm penetration depth times $(100 \mu\text{m})^2$ spot size, 0.66 oxygen atoms on the O-I sites per unit cell volume, time scale of the experiment of 1 h] and comparing it to the Monte Carlo sampling (3×10^7 total simulation steps in a matrix of size 120, occupation $1/3$). For the time scales to match, one in every 10^2 photons would have to move an oxygen atom. Given the restraints mentioned, however, we merely attempt a qualitative description of the effect of light and activation energies on the number of chain fragments and relate it to the behavior of Raman signal decay. But even with this qualitative character our extension of the ASYNINI model provides an understanding of the experimental cooling-illumination-reannealing cycle and explains the form and temperature dependence of chain building and therefore Raman bleaching.

B. Simulation results

Figure 8(g) contains the number of chain fragments during the simulation at low temperatures and under illumination as described in the previous section, from point 2 to 3 in Fig. 7(c). There is good qualitative agreement between experiment and simulations at low temperatures in that the curves display stretched exponential behavior and the most efficient bleaching is at intermediate temperatures. The functional form of the time dependence is a consequence of the type of ordering process. In a situation with many short fragments and single atoms, the probability of reaching an energetically favorable place at a chain end is high, so the initial decrease in fragment number is steep. Beyond the declining number of possibilities for a single atom to join a chain, the growing chains provide stable barriers which are not likely to be crossed, nor to be moved. In the ordering dynamics above room temperature these two different ranges of the type of ordering, building of chains at first and later growth of domains, were identified and described in terms of scaling laws.^{35–38} The actual relaxation times are thus sensitive to the specific local distribution, and they are likely to increase along with the pattern being built, leading to an over exponential slow-down of reordering. This characteristic corresponds to a deeply disordered system with a broad range of relaxation times, resulting in the typical stretched exponential decay as a function of time.³⁴ The observed freeze-out then resembles a critical slowing down of the dynamics rather than a well-defined energy barrier for individual oxygen site hopping, which would be simply exponential ($\beta = 1$). Thus, the form of the decay shows stretched exponential character resulting from the ordering characteristics without any further assumptions.

For a more detailed comparison, parameters from fits analogous to the experimental data are shown in Fig. 9. In Fig. 9(a) the decay times decrease rapidly with increasing temperature, reflecting the exponential change of hopping probability for a single atom. The low-temperature slow down prevents the development of equilibrium within the calculation length chosen, with an effect on the system similar to that of an effective energy barrier.

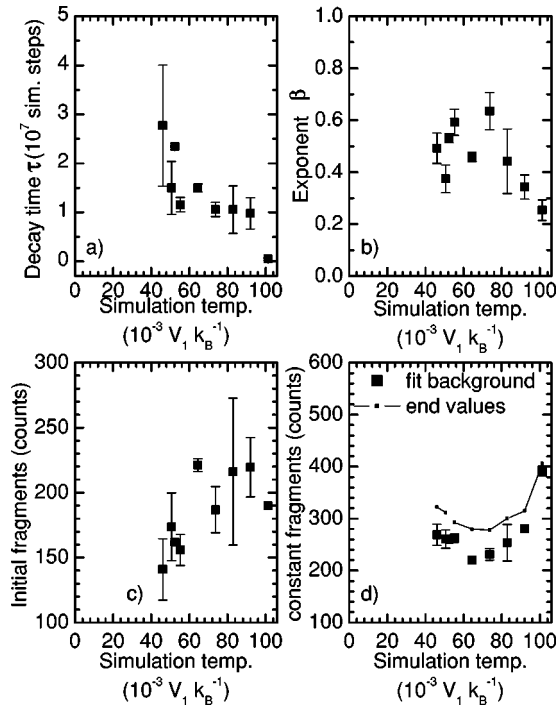


FIG. 9. Parameters from fits with a stretched exponential function to the simulation data versus temperature. (a) Decay time τ , (b) exponent β , (c) initial fragment number, and (d) end fragment number from fit and actual last value of simulation (lines). In some of the simulation fits the background had to be fixed in order to achieve convergence of the fit (symbols without error bars).

The simulations resemble the results for the $\text{YBa}_2\text{Cu}_3\text{O}_{7-\delta}$ material in that there is a dependence of β on temperature [Fig. 9(b)]. The agreement is expected to be better than for $R=\text{Pr}$, as the parameter set with the in-built anisotropy was chosen to match $R=Y$. The change of β could be shifted in temperature by including a second energy barrier against hopping of light-excited oxygen in the model, or by extending the length of the simulations. However, the constraints from the critical slowing down prevented us from further pursuing this aspect.

An explanation for the end values [Fig. 9(d)] also follows naturally: at high temperature the pattern changes faster, but the system is aiming for a less ordered equilibrium state. All end states remain far from the ideal schematic pattern (no fragmentation), so that a further reduction of fragments remains possible. The initial intensity and the background [compare Fig. 4(d)] are remarkably similar to the Raman data.

One feature is not contained in the model: the observed bleaching at room temperature. We assumed light excitation to enhance the oxygen hopping rate at low temperatures. At room temperature, where we are already in equilibrium, switching off an energy barrier does not cause any further relaxation. In the simulations, illumination will therefore not change the order in the system. Room-temperature photoexcitation effects are, however, observed in Raman spectroscopy as well as transport experiments.¹¹ This could be taken into account by assuming that light excitation alters the equilibrium state of the entire system or enhances the probability

of switching to a chain site for individual oxygen atoms. However, we refrained from obscuring the simplicity of the model picture with more parameters.

Summarizing, we set up a model to follow the dynamics of oxygen hopping to neighboring sites in a chain plane of $\text{RBa}_2\text{Cu}_3\text{O}_{7-\delta}$. The interaction energies are defined anisotropically, such that the lattice develops superstructure patterns of chains. For each temperature an equilibrium state exists, where pattern building and thermally induced disorder are balanced. An energy barrier E_B causes the system to remain in nonequilibrium within the simulation time at sufficiently low temperatures. Light eliminates the barrier, reactivating oxygen hopping under illumination at low temperatures. At very low temperatures ($T < 40 \times 10^{-3} V_1/k_B$) critical slowing down sets in, preventing further simulations. A cycle of annealing with the barrier at high temperatures, setting to low temperatures, watching the reformation without barrier, and warming up again, emulates the experimental cooling-illuminating-warming cycle. A qualitative agreement with the functional form and temperature dependence is found. The latter follows directly from the assumption of light triggering reordering into superstructures in a system of frozen-in disorder. The simulations illustrate the changes induced in the material during low-temperature illumination and subsequent thermal annealing. The model and Raman results deviate for room-temperature bleaching, which is not included in the description.

V. CONCLUSIONS

We have investigated the Raman-signal decay of resonant defect-induced modes in oxygen-deficient $\text{YBa}_2\text{Cu}_3\text{O}_{6.7}$ and $\text{PrBa}_2\text{Cu}_3\text{O}_{6.7}$ in the temperature range between 40 and 300 K. We found a temperature dependence of the bleaching with a slow decay for low temperatures and an initially steep and fast decay at high temperatures, which is well described by a stretched exponential function. In contrast to the more tetragonal $\text{PrBa}_2\text{Cu}_3\text{O}_{6.7}$, $\text{YBa}_2\text{Cu}_3\text{O}_{6.7}$ shows a pronounced change in curve shape between 160 and 190 K. We set up Monte Carlo simulations to follow the dynamics of chain-fragment development of oxygen superstructures in the chain plane of $(\text{Y}, \text{Pr})\text{Ba}_2\text{Cu}_3\text{O}_{6.7}$. We found qualitative agreement between simulation and experimental dynamics at low temperatures. At room temperature, the description deviates from the Raman results, as ground-state annealing was not incorporated. Our results support the concept that the Raman-signal decay can be taken as a measure of the structure formation induced by light. Raman spectroscopy combined with a Monte Carlo simulation of oxygen atom hopping thus provides a tool for understanding the dynamics of oxygen atom ordering in high-temperature superconductor materials.

ACKNOWLEDGMENTS

This work was supported by the Deutscher Akademischer Austauschdienst (DAAD) and the Agencia Nacional para la Promoción Científica y Tecnológica of Argentina under the program PROALAR 2000. We acknowledge helpful discussions with J. Guimpel, E. Osquiguil, and S. Reich.

- *Permanent address: ICREA Research Professor, Institut de Ciència de Materials de Barcelona, Campus de la UAB, 08193 Bellaterra, Spain.
- ¹R. Beyers, B. T. Ahn, G. Gorman, V. Y. Lee, S. S. P. Parkin, M. L. Ramirez, K. P. Roche, J. E. Vazquez, T. M. Gür, and R. A. Huggins, *Nature* (London) **340**, 619 (1989).
 - ²B. W. Veal, H. You, A. P. Paulikas, H. Shi, Y. Fang, and J. W. Downey, *Phys. Rev. B* **42**, 4770 (1990).
 - ³J. D. Jorgensen, S. Pei, P. Lightfoot, H. Shi, A. P. Paulikas, and B. W. Veal, *Physica C* **167**, 571 (1990).
 - ⁴B. W. Veal, A. P. Paulikas, H. You, H. Shi, Y. Fang, and J. W. Downey, *Phys. Rev. B* **42**, 6305 (1990).
 - ⁵N. H. Andersen, M. von Zimmermann, T. Frello, M. Käll, D. Mønster, P. A. Lindgård, J. Madsen, T. Niemöller, H. F. Poulsen, O. Schmidt, J. R. Schneider, T. Wolf, P. Dosanjh, R. Liang, and W. N. Hardy, *Physica C* **317-318**, 259 (1999).
 - ⁶T. Krekels, H. Zou, G. V. Tendeloo, D. Wagener, M. Buchgeister, S. M. Hosseini, and P. Herzog, *Physica C* **196**, 363 (1992).
 - ⁷T. Frello, N. H. Andersen, J. Madsen, A. B. Abrahamsen, M. von Zimmermann, T. Niemöller, J. R. Schneider, and T. Wolf, *Phys. Rev. B* **61**, R9253 (2000).
 - ⁸A. A. Aligia and J. Garcés, *Phys. Rev. B* **49**, 524 (1994).
 - ⁹S. Sadewasser, Y. Wang, J. S. Schilling, H. Zheng, A. P. Paulikas, and B. W. Veal, *Phys. Rev. B* **56**, 14 168 (1997).
 - ¹⁰A. I. Kirilyuk, N. M. Kreines, and V. I. Kudinov, *JETP Lett.* **52**, 49 (1990).
 - ¹¹G. Nieva, E. Osquiguil, J. Guimpel, M. Maenhoudt, B. Wuyts, Y. Bruynseraede, M. B. Maple, and I. K. Schuller, *Appl. Phys. Lett.* **60**, 2159 (1992).
 - ¹²V. I. Kudinov, I. L. Chaplygin, A. I. Kirilyuk, N. M. Kreines, R. Laiho, E. Lähderanta, and C. Ayache, *Phys. Rev. B* **47**, 9017 (1993).
 - ¹³J. F. Federici and D. M. Bubb, *J. Supercond.* **14**, 331 (2001).
 - ¹⁴W. Markowitsch, C. Stockinger, W. Göb, W. Lang, W. Kula, and R. Sobolewski, *Physica C* **265**, 187 (1996).
 - ¹⁵D. R. Wake, F. Slakey, M. V. Klein, J. P. Rice, and D. M. Ginsberg, *Phys. Rev. Lett.* **67**, 3728 (1991).
 - ¹⁶V. G. Hadjiev, C. Thomsen, J. Kircher, and M. Cardona, *Phys. Rev. B* **47**, 9148 (1993).
 - ¹⁷A. Fainstein, P. Etchegoin, and J. Guimpel, *Phys. Rev. B* **58**, 9433 (1998).
 - ¹⁸A. G. Panfilov, A. I. Rykov, S. Tajima, and A. Yamanaka, *Phys. Rev. B* **58**, 12 459 (1998).
 - ¹⁹M. Käll, M. Osada, M. Kakihana, L. Börjesson, T. Frello, J. Madsen, N. H. Andersen, R. Liang, P. Dosanjh, and W. N. Hardy, *Phys. Rev. B* **57**, R14 072 (1998).
 - ²⁰A. Fainstein, B. Maiorov, J. Guimpel, G. Nieva, and E. Osquiguil, *Phys. Rev. B* **61**, 4298 (2000).
 - ²¹S. Bahrs, A. R. Goñi, C. Thomsen, B. Maiorov, G. Nieva, and A. Fainstein, *Phys. Rev. B* **65**, 024522 (2002).
 - ²²P. Nagel, V. Pasler, C. Meingast, A. I. Rykov, and S. Tajima, *Phys. Rev. Lett.* **85**, 2376 (2000).
 - ²³H. F. Poulsen, N. H. Andersen, J. V. Andersen, H. Bohr, and O. G. Mouritsen, *Nature* (London) **349**, 594 (1991).
 - ²⁴D. Mønster, P.-A. Lindgård, and N. H. Andersen, *Phys. Rev. B* **60**, 110 (1999).
 - ²⁵D. Mønster, P. A. Lindgård, and N. H. Andersen, *Phys. Rev. B* **64**, 224520 (2001).
 - ²⁶P. Manca, S. Sanna, G. Calestani, A. Migliori, S. Lapinskas, and E. E. Tornau, *Phys. Rev. B* **63**, 134512 (2001).
 - ²⁷M. von Zimmermann, J. R. Schneider, T. Frello, N. H. Andersen, J. Madsen, M. Käll, H. F. Poulsen, R. Liang, P. Dosanjh, and W. N. Hardy, *Phys. Rev. B* **68**, 104515 (2003).
 - ²⁸K. Kawamoto and I. Hirabayashi, *Phys. Rev. B* **49**, 3655 (1994).
 - ²⁹R. Liu, C. Thomsen, W. Kress, M. Cardona, B. Gegenheimer, F. W. de Wette, J. Prade, A. D. Kulkarni, and U. Schröder, *Phys. Rev. B* **37**, 7971 (1988).
 - ³⁰V. G. Ivanov, M. N. Iliev, and C. Thomsen, *Phys. Rev. B* **52**, 13 652 (1995).
 - ³¹S. Bahrs, A. R. Goñi, B. Maiorov, G. N. Nieva, A. Fainstein, and C. Thomsen, *IEEE Trans. Appl. Supercond.* **13**, 3192 (2003).
 - ³²E. F. Righi, S. A. Grigera, G. Nieva, and F. de la Cruz, *Supercond. Rev.* **2**, 205 (1998).
 - ³³E. Osquiguil, M. Maenhoudt, B. Wuyts, and Y. Bruynseraede, *Appl. Phys. Lett.* **60**, 1627 (1992).
 - ³⁴H. Scher, M. F. Shlesinger, and J. T. Bendler, *Phys. Today* **44**(1), 26 (1991).
 - ³⁵H. F. Poulsen, N. H. Andersen, J. V. Andersen, H. Bohr, and O. G. Mouritsen, *Phys. Rev. Lett.* **66**, 465 (1991).
 - ³⁶P. J. Kundrotas, E. E. Tornau, and A. Rosengren, *Phys. Rev. B* **54**, 4357 (1996).
 - ³⁷M. Käll, M. von Zimmermann, N. H. Andersen, J. Madsen, T. Frello, H. F. Poulsen, J. R. Schneider, and T. Wolf, *Europhys. Lett.* **51**, 447 (2000).
 - ³⁸P. Schleger, R. A. Hadfield, H. Casalta, N. H. Andersen, H. F. Poulsen, M. von Zimmermann, J. R. Schneider, R. Liang, P. Dosanjh, and W. N. Hardy, *Phys. Rev. Lett.* **74**, 1446 (1995).